Check for updates

Advanced Energy Materials

ADVANCED ENERGY MATERIALS
www.advenergymat.de

RESEARCH ARTICLE OPEN ACCESS

Influence of Metal Species and Content of Fe-Ni-Poly(heptazine imides) on their Properties as Electrocatalysts for Zinc-Air Batteries

Franz Jacobi[1] | Rudolf Frank Baumgart[1] | Robert Leiter[3,4] | Marius Hermesdorf[1] | Sri Rezeki[1] | Alexander Kemmesies[5] | Christof Neumann[2] | Andrey Turchanin[2,6] | Christopher Schlesiger[5] | Simon Fleischmann[3,4] | Desirée Leistenschneider[1,6]

[1]Institute for Technical and Environmental Chemistry, Friedrich-Schiller University Jena, Jena, Germany | [2]Institute of Physical Chemistry, Friedrich-Schiller University Jena, Jena, Germany | [3]Helmholtz Institute Ulm (HIU), Ulm, Germany | [4]Karlsruhe Institute of Technology (KIT), Karlsruhe, Germany | [5]Institute of Physics and Astronomy, Technical University Berlin, Berlin, Germany | [6]Center for Energy and Environmental Chemistry (CEEC) Jena, Friedrich-Schiller University Jena, Jena, Germany

Correspondence: Desirée Leistenschneider (desiree.leistenschneider@uni-jena.de)

Received: 7 November 2025 | **Revised:** 22 December 2025 | **Accepted:** 1 January 2026

Keywords: noble metal-free | oxygen reduction reaction | oxygen evolution reaction | Poly(heptazine imide) | zinc-air battery

ABSTRACT

Alkaline zinc-air batteries (ZABs) have attracted interest in recent years for their high theoretical energy density and use of low-cost, abundant zinc metal as the anode. In order to overcome the activation energy barrier of the oxygen reduction reaction (ORR) and oxygen evolution reaction (OER), noble metals are commonly used. Within this work, transition metal-functionalized Poly(heptazine imide)s (PHIs) are studied as an alternative and more abundant electrocatalyst, as they offer the homogenous immobilization of metals within their ordered structure. Introducing Fe and Ni into the PHI network enables the formation of single and mixed transition metal PHIs, which show reduced overpotentials for ORR and OER. The formation of Ni single atoms even induces outstanding catalytic activity for the OER during charging of ZAB full cells with performance comparable to that of RuO_2. Furthermore, full cell tests show excellent stability over the course of 250 discharge-charge cycles, making it a promising system for sustainable energy storage. This work paves the way for the molecular design of a novel material class as an electrocatalyst for ZAB.

1 | Introduction

Around 1800, Alessandro Volta reported the first battery that converted chemical energy into electric energy [1]. This technology led to the innovation of further primary batteries such as the Daniel element, which were used for electric powering and exhibited high energy densities - until the discovery of the generator [2]. However, due to the electrification of today's society, such high-energy density battery systems are gaining more and more importance. In particular, batteries that are portable, safe, non-toxic, and ideally based on abundant resources. Among others, the zinc-air battery (ZAB) is a great candidate for such requirements, as it utilizes low-cost, highly-available zinc metal for the anode and is generally regarded as a non-toxic and safe battery system [3, 4]. Furthermore, they bear a high theoretical specific energy density of ≈1350 $Whkg^{-1}$, making them attractive for applications calling for a long-term steady energy output. To this day, energy densities of ≈200 $Whkg^{-1}$ can be reached in practice, marking the true potential of the ZAB yet to unfold [3, 5–7].

This is an open access article under the terms of the Creative Commons Attribution License, which permits use, distribution and reproduction in any medium, provided the original work is properly cited.

© 2026 The Author(s). *Advanced Energy Materials* published by Wiley-VCH GmbH

Several challenges for designing high-performing rechargeable ZABs exist, such as Zn dendrite formation or carbonate and oxide precipitation [3]. This work, however, will focus on the oxygen reduction reaction (ORR) and oxygen evolution reaction (OER), which govern the charge and discharge process, as they suffer from sluggish kinetics and high overpotentials. To overcome this issue, carbon-supported noble metals like Pt or Pd are employed [7–9]. As the use of such scarce elements hinders economically efficient large-scale production, there is a growing need for more sustainable and available catalyst materials.

Although zinc is generally more abundant, it frequently poses a local environmental risk by harming biodiversity and ecosystems through mining and refining processes [10]. Therefore, it is imperative to place its sustainable use in such battery systems at the forefront of development efforts. One approach is the design of rechargeable ZABs, which enable a longer lifetime of battery cells and a more sustainable use of Zn as a metal.

Rechargeability can be realized by the use of catalysts that overcome overpotentials for the oxygen evolution reaction at the cathode side. Generally, catalysts such as RuO_2 or IrO_2 are deposited onto the gas diffusion layer (GDL) additionally to the ORR catalysts. However, as already mentioned, the use of noble metals contradicts the original motivation of a sustainable battery. Sustainable alternatives for such catalysts are based on carbon, nitrogen, and earth-abundant transition metals (TM) [11–13].

A promising candidate for the development of new catalyst materials is poly(heptazine imide) (PHI), a member of the ionic carbon nitride family [14]. Structurally, ionic PHIs are closely related to graphitic carbon nitride melon - discovered in 1834 by Justus von Liebig - and the covalent, metal-free poly(heptazine imide) [15, 16]. That said, ionic PHIs - or metal PHIs (M-PHIs) - incorporate metal cations within their structure, which are counterbalanced by negatively charged imide bridges. Those cations enable the long-range order of M-PHIs, their ionic conductivity, as well as their tailorable photoelectrochemical properties. A well-investigated M-PHI is K-PHI with K^+ ions integrated in its structure [17–22]. Those metal cations can be substituted by other ionic species such as TM, ionic liquids, or protons. For that reason, M-PHIs bear the nickname “organic zeolites” [17, 23, 24].

Since the K^+ ions in K-PHI are well-distributed into the network, substitution with catalytically active TM allows for the generation of single-atom catalysts, which are a promising class of catalyst materials for their controllable electronic band structure, highly-exposed metal centers, and high atom efficiency [25–27]. Introduction of TM can be achieved in a facile aqueous ion-exchange reaction. This allows for adjusting the desired metal content and immobilizes the metal within the PHI network by chelating the effects of N vacancies [14, 26, 28, 29]. As photocatalysts, M-PHIs have been applied for the aqueous hydrogen evolution reaction (HER) and oxygen reduction reaction (ORR), organic synthesis and pollutant degradation, to name a few [30–35]. So far, only a few publications report the use of M-PHIs as electrocatalysts. For example, Ye et al. utilized Co-PHI as an electrocatalyst for the OER toward application in fuel cells [14]. Zhao et al. investigated the capability of TM doped PHIs for electrochemical nitrogen reduction reaction by density functional theory calculations, and found Mo-PHI to be a promising candidate [26].

In this work, Fe- and Ni-functionalized PHIs are utilized as electrocatalysts in ZAB, substituting Pd and RuO_2, respectively. Since PHIs have not been thoroughly explored for reducing overpotentials in electrochemical ORR and OER, the effect of different metal loadings as well as Ni/Fe dual-functionalization, on the overpotential is investigated, both in half-cell measurements and in ZAB full cells. This work employs the potential of PHIs as electrocatalysts in ZAB and paves the way for their further application as noble metal alternatives.

2 | Results and Discussion

2.1 | Synthesis of K-PHI and Ion Exchange Reaction

Single TM PHIs were obtained from a three-step synthetic procedure (Figure S1). In summary, melamine was thermally polymerized to melon under inert conditions in the first step [23, 24]. Then, melon was converted to K-PHI via ionothermal synthesis using KSCN [21]. Crude K-PHI is then thoroughly washed with deionized water to remove KSCN. During workup, the formation of solvated K-PHI can be observed (Figure S2).

The obtained K-PHI further serves as the starting material for the synthesis of single TM M-PHIs (Figure S3). For this purpose, aqueous ion-exchange reactions were performed with ferrous chloride ($FeCl_2{\cdot}4H_2O$) as Fe^{2+} source, ferric chloride ($FeCl_3{\cdot}6\ H_2O$) as Fe^{3+} source, and anhydrous nickel chloride ($NiCl_2$) dissolved in deionized water, respectively [17]. Depending on whether 10 or 50 mM metal salt solutions were used during synthesis, the M-PHIs were denoted as M-PHI-10 or M-PHI-50 (Figure S1).

2.2 | Bonding Behavior of Single Metals within the PHI Network

To gain insight into the long-range order of the obtained materials, powder X-ray diffraction (PXRD) measurements were carried out with melon, K-PHI, and the M-PHI-50 materials (Figure 1a,b). It is hypothesized that the integration of TM into the PHI network could potentially alter the structure of PHIs by changing coulombic interactions and thus the interlayer spacing of the PHI sheets by cation intercalation. In melon, a characteristic reflex can be found at 27.5° 2θ, corresponding to the layer stacking of the melon sheets [36]. Using Bragg’s equation (Section S2.2.1), this corresponds to an interlayer distance of 3.24 Å. Additionally, a broad signal observed at ≈13° 2θ can be assigned to the in-plane repeating heptazine units with distances of ≈6.75 Å [21, 36]. Conversion of melon to K-PHI results in a decrease of the interlayer distances as observed by an increase of diffraction angle by ≈1° 2θ, corresponding to PHI sheet distances of ≈3.14 Å. This observation underlines the role of K^+ as a stacking mediator and is in good accordance with the literature [23]. Integration of TM into the PHI network by aqueous ion exchange does not result in an apparent major change of the PXRD patterns in the low-angle range. All patterns show a reflex corresponding to the interlayer stacking, confirming that the PHI network remains intact after ion exchange. After cation exchange, slight changes of the interlayer stacking reflex are observed (Figure

16146840, 0, Downloaded from https://advanced.onlinelibrary.wiley.com/doi/10.1002/aenm.202506308, Wiley Online Library on [05/02/2026]. See the Terms and Conditions (https://onlinelibrary.wiley.com/terms-and-conditions) on Wiley Online Library for rules of use; OA articles are governed by the applicable Creative Commons License

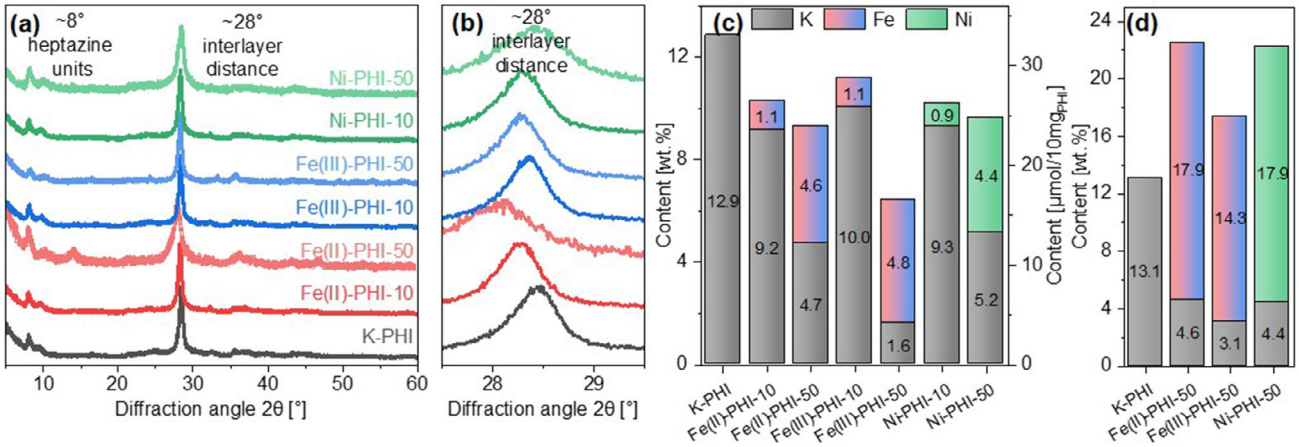

FIGURE 1 | (a) PXRD diffractograms of melon, K-PHI, and M-PHI. (b) Excerpt of stacked PXRD of melon, K-PHI, and M-PHI. (c) Absolute molar metal content and relative metal content of K-PHI and the M-PHIs were determined by ICP-OES. (d) Relative metal content of K-PHI and M-PHI-50 determined by XPS.

S4a). Generally, the reflex is shifted slightly by 0.05° 2θ to lower angles in comparison to K-PHI. This points to a minor increase in interlayer distance when functionalizing with Fe or Ni by ≈0.01 Å. What is even more pronounced are the increases in width of the reflex when more metal is introduced in the structure, pointing toward a decrease in long-range order, or the peak broadens due to smaller areas that coherently scatter.

Therefore, the sizes of coherently scattering domains within the PHI materials were calculated using the Scherrer equation (Table S6). Here, the sizes of K-PHI and the M-PHIs are ≈18 nm with the exception of Fe(II)-PHI-50 with ≈8 nm and Ni-PHI-50 with ≈10 nm (Figure S4b), as already suspected. As the metal ion solutions are fairly acidic, it could be hypothesized that partial conversion from K-PHI to H-PHI occurs, resulting in a decrease of crystallite size as observed by Schlomberg et al. [23]. However, as hydrated Fe^{3+} is more acidic than hydrated Fe^{2+}, smaller crystallites should be observable for Fe(III)-PHI-10, which is not the case. Therefore, it is more plausible that Fe^{2+} and Ni^{2+} at higher concentrations decrease the long-range order of the material by increased exfoliation of the PHI sheets. Additionally, the long-range order of the material is also represented in the relatively low BET surface area compared to porous carbons i.e., (Figure S5).

In order to quantify the bulk metal ion content of the M-PHIs, inductively coupled plasma optical emission spectroscopy (ICP-OES) was performed (Figure 1c). Since K-PHI was thoroughly washed prior to the ion exchanges, it can be assumed that no residual KSCN is present within the material. This is supported by the absence of KSCN reflexes in the PXRD diffractogram (Figure 1a). Ion exchange of K-PHI with TM results in a decrease of K^+ content and simultaneously the increase of TM content (Figure 1c). The weight fraction of the TM lies at ≈1 wt.% for the M-PHI-10 and at ≈5 wt.% for the M-PHI-50. This shows that the concentration of the metal solution used for the ion exchange directly influences the final metal content. This is further illustrated by the successive ion exchange of K-PHI with Fe (Figure S6). The multi-valency of the TM hereby plays an important role, as the release of K^+ from the material presumably results in an increase of the overall entropy and is therefore a driving force for the reaction. By conversion of the weight fraction to a molar fraction, the amount of K^+ released and TM introduced to the network can be compared (Figure 1c). Here, it can be observed that the amount of K^+ displaced from the PHI network is higher than the amount of TM cation introduced that would balance the charge, suggesting that other cations, most likely H^+, are additionally introduced to the network (Section S3.2.1).

To better understand whether the TM is distributed homogenously within the PHI network or if differences can be observed between bulk and surface metal concentration, XPS measurements were carried out with K-PHI and M-PHI-50, as it is a surface-sensitive method (Figure 1d). In K-PHI, the amount of K^+ at the surface is equivalent to the bulk material at ≈13 wt.%. After the ion exchange, the content of K^+ at the surface decreases to 3 wt.% in Fe(III)-PHI-50 and to 4.5 wt.% in Fe(II)-PHI-50 and Ni-PHI-50. After ion exchange, the TM content amounts to 14 wt.% in Fe(III)-PHI-50 and to 18 wt.% in Fe(II)-PHI-50 and Ni-PHI-50. Here, in contrast to the bulk content derived from ICP-OES, the amount of TM is significantly higher at the PHI surface. This indicates that the functionalization with TM mainly occurs at the PHI surface.

To gain insight into the bonding conditions within the PHIs, Fourier transform infrared spectroscopy (FT-IR) was performed in addition to XPS measurements (Figure S7a,b). The FT-IR spectra reveal the typical signals for PHI materials, such as the out-of-plane heptazine bending at 800 cm^{-1}, the valence stretching of the heptazine units at 1200–1700 cm^{-1}, as well as a signal located at 2170 cm^{-1} belonging to cyanamide end groups, which are a known structural feature within the PHI network [22]. Additionally, a slight shift of the signal at ~800 cm^{-1} indicates a change in N-M bonding due to ion exchange [14, 17, 28].

In addition, the XPS spectra of K-PHI and M-PHI were superimposed (Figure 2b–d). The K2p signal at 297-291 eV indicates a decrease of K^+ ions at the surface of the PHI after ion exchange. At 290-286 eV the C=N signal can be found relating to the heptazine ring (Figure 2b). For K-PHI, the maximum of this signal lies at 287.9 eV. Here, a slight shift toward higher binding

16146840, 0, Downloaded from https://advanced.onlinelibrary.wiley.com/doi/10.1002/aenm.202506308, Wiley Online Library on [05/02/2026]. See the Terms and Conditions (https://onlinelibrary.wiley.com/terms-and-conditions) on Wiley Online Library for rules of use; OA articles are governed by the applicable Creative Commons License

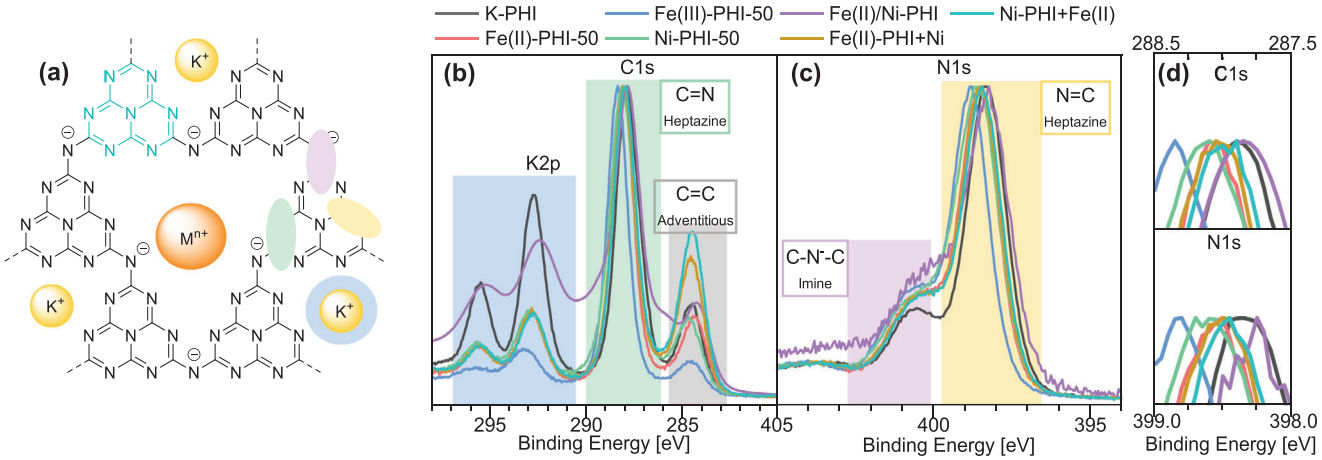

FIGURE 2 | (a) Scheme describing the chemical structure of an M-PHI layer. (b) Normalized XPS spectra of the C1s and K2p signal of K-PHI, M-PHI-50, and mixed metal PHIs. (c) Superimposed, normalized XPS spectra of the N1s signal of K-PHI, M PHI-50, and mixed metal PHIs. (d) Close-up view of (b) and (c), indicating the shift of the photoelectron emission maximum.

energies is notable for Fe(III)-PHI-50 at 288.4 eV, indicating a decrease of electron density at the heptazine C caused by the electron-withdrawing effect of Fe^{3+} coordinating to heptazine N. This effect is also observable for Fe(II)-PHI-50 and Ni(II)-PHI-50, whose signals lie at 288.1 eV, slightly lower than Fe(III)-PHI-50. Additionally, a C═C signal at 284.8 eV is observed, likely relating to adventitious carbon, a typical XPS signal caused by hydrocarbon adsorption at ambient [37]. The presence of adventitious C is also indicated by the differing C: N ratios of XPS and combustion analysis (Figure S8).

The N1s signal can be divided into the C—N—C imine region at binding energies of 402-400 eV and into the N═C heptazine region at 400-396 eV (Figure 2c). For K-PHI, the maximum in the N═C region lies at 398.4 eV, while for Fe(III)-PHI-50 it lies at 398.8 eV, caused by the decrease of electron density at the heptazine N due to Fe^{3+} coordination. Less shifting is observable for Fe(II)-PHI-50 and Ni-PHI-50 at 398.6 eV due to lower electron-withdrawing effects. This observation further strengthens the different coordination of metals due to their varying oxidation states and numbers of coordination sites.

As Fe2p and Ni2p spectra are difficult to evaluate due to low signal-to-noise ratio and complex satellite structure of transition metals, the oxidation states and bonding environments of the metals within the M-PHIs were further studied via X-ray absorption near edge structure spectroscopy (XANES) and extended X-ray absorption fine structure spectroscopy (EXAFS), respectively (Figure 3a–d; Full spectra shown in Figure S9). The position of the absorption edge in this context gives insights into the oxidation state and electronic structure of the examined atom. In addition, the specific chemical environment also has an effect on the position of the absorption effect; hence, having appropriate reference materials is of high importance. Therefore, different reference materials such as Fe foil, $FeCl_2 \cdot 4H_2O$, $FeCl_3 \cdot 6H_2O$, and $[Fe(tpy)_2]Cl_2$ were chosen, with the latter representing the coordination environment within the PHI network the closest.

In this context, both Fe(II)-PHI-50 and Fe(III)-PHI-50 show nearly identical K edge absorption edges at ≈7125 eV, which compare to those of $FeCl_3 \cdot 6H_2O$ and the Fe terpyridine complex (Figure 3a). As Fe^{2+} is present in both $FeCl_2 \cdot 4H_2O$ and $[Fe(tpy)_2]^{2+}$ while the K edge of the latter is shifted to higher energies, the role of the coordination environment close to the Fe atom is emphasized. Prior studies show that Fe is coordinated to N moieties within the PHI structure [28]. Therefore, comparison to $[Fe(tpy)_2]^{2+}$ as a reference compound is logical. Still, comparison of the K edge shifts of Fe(II)-PHIs and Fe(III)-PHIs does not allow for clear differentiation between the Fe^{2+} and Fe^{3+} oxidation states. Furthermore, it is possible that Fe^{2+} is oxidized to Fe^{3+} during the aqueous ion exchange or over prolonged air contact.

EXAFS analysis gives insights into the bonding environment of the different element edges investigated due to interference effects of the photoelectron with itself scattered at neighboring atoms. The FT-EXAFS shows a strong signal, i.e., a high amplitude at distances of coordination spheres that can ideally be compared with forward calculations of input crystal structures. Here, we rely on a purely comparative approach with reference materials without using crystal structures (such as .cif files). This way, the coordination environment and the absence of metal-metal bonds can be estimated. In this context, peak positions of the first coordination shells of the PHIs and $[Fe(tpy_2)]Cl_2$ range around ≈1.3–1.4 Å, which is lower than in the Fe chloride salts or Fe foil references (Figure 3b). This also suggests the presence of Fe-N bonds and ensures that no Fe-Fe bonds at ≈2.2 Å are present due to the spatially separated coordination sites of the PHI network. All Fe-PHIs show such bonding behavior, emphasizing the coordination of Fe to the N-moieties within the PHI backbone. Since the intensity of the EXAFS signal at 1.3–1.4 Å of the PHIs and $[Fe(tpy)_2]Cl_2$ is comparable and assuming similar elements in the vicinity, Fe is likely coordinated by six atoms within the PHI scaffold. Higher coordination spheres, on the other hand, as represented by the signal at 2.2 Å for $[Fe(tpy)_2]Cl_2$ and at 2.6 Å for the PHIs, indicate the chemical dissimilarity between the PHIs and the reference materials and thus the limited comparability.

Here, it should also be noted that additional signals can be observed at ≈2.5-2.7 Å. Those signals may derive from multiple

16146840, 0, Downloaded from https://advanced.onlinelibrary.wiley.com/doi/10.1002/aenm.202506308, Wiley Online Library on [05/02/2026]. See the Terms and Conditions (https://onlinelibrary.wiley.com/terms-and-conditions) on Wiley Online Library for rules of use; OA articles are governed by the applicable Creative Commons License

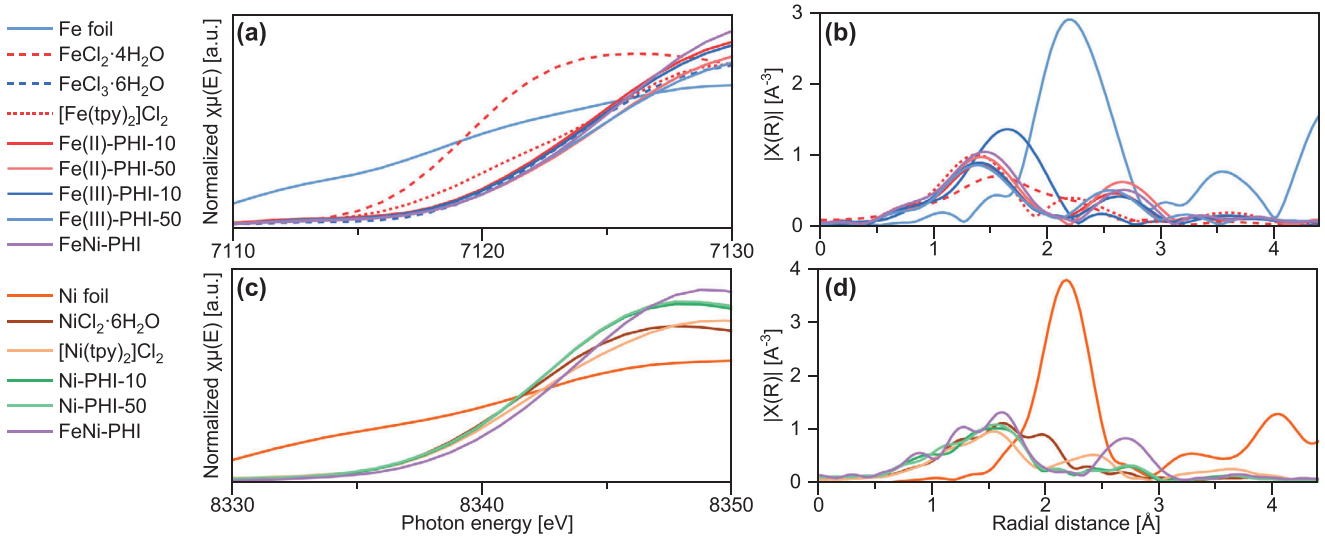

FIGURE 3 | Excerpts of (a) K-edge XANES of the Fe absorption edge of Fe references and Fe containing PHI samples. (b) Fourier transformed EXAFS of Fe references and Fe containing PHI samples. (c) K edge XANES of the Ni absorption edge of Ni references and Ni containing PHI samples. (d) Fourier transformed EXAFS of Ni references and Ni containing PHI samples (full spectra available in Figure S8).

scattering within the sample or correlate to higher coordination shells or a combination of both. Also, the bonding distances derived from the EXAFS data must not directly correlate to a certain bonding distance, as structural properties of the materials have to be considered for that.

For Ni-PHI, the absorption edges of all materials lie at ≈8342 eV and thus relatively close to each other (Figure 3c). In contrast to the Fe-PHIs, the position of the absorption edges of Ni-PHI-10 and Ni-PHI-50 is nearly identical. The Ni-N bond lengths of $[Ni(tpy)_2]Cl_2$ and Ni-PHI-50 lie at ≈1.5 Å as seen in the EXAFS data (Figure 3d). For Fe(II)/Ni-PHI, two local maxima are observable at ≈1.3 and 1.6 Å, which could hint that multiple Ni species are present within the PHI, possibly at negatively charged imide bridges and at the heptazine or vacant cyanamide groups. Similar to the Fe-PHIs, no Ni-Ni bond can be observed as in Ni foil at 2.2 Å, but additional scattering reflexes are observed at ≈2.5-2.7 Å.

2.3 | Investigation of Oxygen Reduction and Oxygen Evolution Activity

To investigate the ORR and OER activities of the PHI materials, linear sweep voltammetry (LSV) was performed in alkaline electrolyte on carbon cloth with the addition of a conductive additive to ensure good charge transport (Figure S10). For this purpose, impedance spectroscopy and ten LSVs were recorded in succession for priming of the electrode and to ensure complete wetting of the electrode surface (Figures S11 and S12). Here, Pd/C served as a reference for the ORR activity and RuO_2 for the OER activity. To compare the activities of the materials, the onset potential was defined as the potential at which a current density of 10 $mAcm^{-2}$ is reached in the tenth measurement [38].

For the ORR, the benchmark catalyst Pd/C shows an onset potential of 0.777 mV vs RHE (Figure 4a, Table 1). K-PHI, Fe(II)-PHI-10, and Fe(III)-PHI-10 show lower onset potentials at ≈0.696 V. Notably, Ni-PHI-10 has a significantly lower onset potential at 0.632 V. In contrast, M-PHI-50 does not reach the current density threshold of 10 $mAcm^{-2}$, which points to no ORR activity of PHIs with higher metal loadings. This has been seen for PHIs in photocatalysis as well, which is why it is desired to fabricate PHIs with rather low metal loadings. Reasons for that, among others, could be the low intrinsic resistance of the material, the change of band gap, or the slower kinetics of the ORR [39]. Although the M-PHIs do not reach the activity of the state-of-the-art material Pd/C, Fe(II)-PHI-10 exhibits the most promising activity toward application for the ORR within a ZAB setup. This result is anticipated, as Fe-N-C catalysts are also of current research interest due to their ORR activity [40, 41]. Additionally, ORR experiments with K-PHI in Ar saturated electrolyte confirm that no hydrogen evolution occurs in the examined potential window (Figure S12). In order to investigate whether the ORR takes place via the $2e^-$ or $4e^-$-pathway, RDE measurements were performed with Fe(II)-PHI-10 and Ni PHI-10 (Figure S13, Table S8). In this context, the obtained results suggest Fe-doping mediates the $4e^-$-pathway, while the addition of Ni promotes the $2e^-$-pathway.

For the OER, more diverse activities can be observed for the PHI materials (Figure 4b). To substantiate that the increase in electrochemical performance results from metal doping instead of a pure increase in electrochemical surface area, the electric double-layer capacitance was determined in addition (Figure S14). With the exception of K-PHI and Fe(II)-PHI-10, all PHI materials reach the current density threshold of 10 $mAcm^{-2}$. Here, the highest activity can be observed for Ni-PHI-10 at an onset potential of 1.629 V, even reaching higher currents than the benchmark catalyst RuO_2 at higher potentials. Interestingly, this contrasts the significantly lower onset potential during the ORR in comparison to K-PHI, Fe(II)-PHI-10, and Fe(III)-PHI-10. This suggests that Ni-PHI-10 is more affine for OH^- than O_2, as the latter is a much weaker ligand. Regarding Fe-PHIs, generally higher activities are notable for Fe(III)-PHIs in

16146840, 0, Downloaded from https://advanced.onlinelibrary.wiley.com/doi/10.1002/aenm.202506308, Wiley Online Library on [05/02/2026]. See the Terms and Conditions (https://onlinelibrary.wiley.com/terms-and-conditions) on Wiley Online Library for rules of use; OA articles are governed by the applicable Creative Commons License

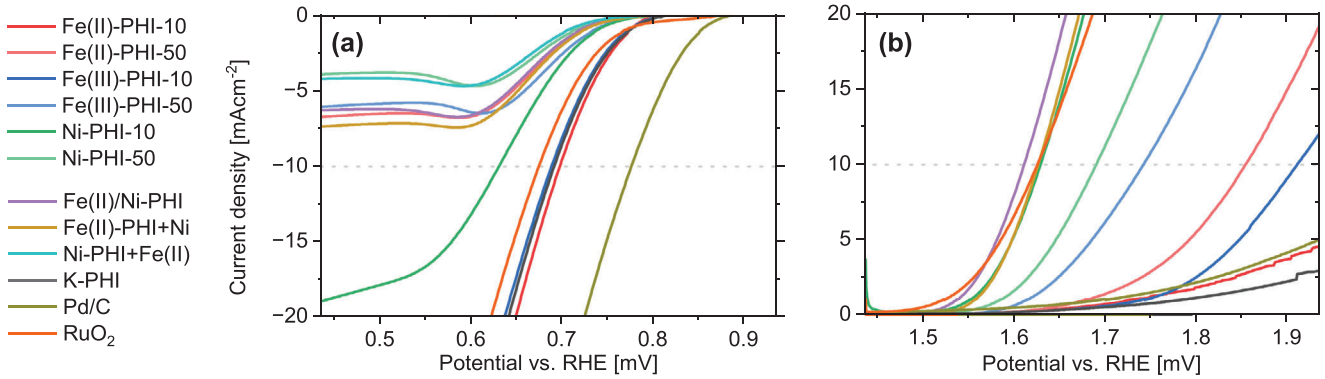

FIGURE 4 | (a) ORR and (b) OER polarization curves of K-PHI, transition metal doped PHIs, and Pd/C and RuO_2 references obtained at a scan rate of 5 mVs^{-1}. Depicted is the tenth LSV curve.

TABLE 1 | Onset potentials of the PHIs for the ORR and OER. The onset potential is defined as the potential where a current density of ± 10 $mAcm^{-2}$ is reached.

	Onset potential vs. RHE [V]	
Material	**ORR**	**OER**
K-PHI	0.693	—
Fe(II)-PHI-10	0.698	—
Fe(II)-PHI-50	—	1.853
Fe(III)-PHI-10	0.690	1.910
Fe(III)-PHI-50	—	1.741
Ni-PHI-10	0.632	1.629
Ni-PHI-50	—	1.690
Fe(II)/Ni-PHI	—	1.626
Fe(II)-PHI+Ni	—	1.611
Ni-PHI+Fe(II)	—	1.626
Pd/C	0.777	—
RuO_2	0.677	1.625

contrast to Fe(II)-PHIs. This indicates Fe^{3+} as the preferable oxidation state for lowering overpotentials for the OER. A possible explanation for this observation is the stronger Lewis acidity and therefore higher OH^- affinity of Fe^{3+}, lowering the activation barrier due to faster adsorption. For Ni, however, lower metal concentrations are favorable, similar to the OER activity of Co-PHI as shown by Ye et al. previously [14]. Conclusively, this highlights Ni-PHI-10 as the most promising single TM PHI material for application as the OER catalyst in a ZAB setup.

2.4 | Mixed Transition Metal PHI Synthesis and Characterization

Investigating the ORR and OER activity of M-PHIs revealed that the introduction of Fe^{2+} and Ni^{2+} into the PHI network decreases overpotentials for the ORR and OER, respectively. Therefore, mixed-TM PHIs were synthesized, introducing both Fe^{2+} and Ni^{2+} to the PHI network simultaneously.

The synthetic procedure for obtaining mixed-metal PHIs is based on the aqueous ion exchanges described previously. Here, two different approaches were followed for obtaining mixed-metal PHIs, namely, simultaneous ion exchange and successive ion exchange. The product of the simultaneous ion exchange is denoted as Fe(II)/Ni-PHI, and the successively exchanged PHIs as Fe(II)-PHI+Ni and Ni-PHI+Fe(II), respectively (Figure S1).

Metal content analysis via ICP-OES was conducted for the mixed-metal PHIs. It can be observed that Fe^{2+} and Ni^{2+} are introduced in equal amounts during the simultaneous ion exchange, yielding metal contents of ≈1 wt.% each in Fe(II)+Ni-PHI (Figure S15). More diverse results are obtained with the successively exchanged PHIs. In Fe(II)-PHI+Ni, the amount of Fe^{2+} is notably higher than Ni^{2+} and vice versa; Ni-PHI+Fe(II) yields higher Ni^{2+} content. It is important to note that the Fe(II)-PHI-10 and Ni-PHI-10 intermediate products are separate batches from the single-TM materials described previously, explaining the slight differences in metal content. In addition, XPS analysis was performed to investigate the surface metal content of the mixed-metal PHIs (Figures S16 and S17). For Fe(II)/Ni-PHI, Fe and Ni were exchanged simultaneously. Here, the content of Fe and Ni lies at 5.3 and 4.8 wt.%, respectively, while the content of K amounts to 9.7 wt.%. In the starting material K-PHI, the content of K was found to be 13.1 wt.%, so the decrease of K content is relatively low. This might be explained by the formation of metal oxide at the PHI surface and should be investigated in more detail in the future. In Fe(II)-PHI+Ni, Fe was introduced in the first step and Ni in the second step. Here, the Fe and Ni contents amount to 3.4 and 1.8 wt.%, respectively. Less Ni is added to the system after Fe is added in the first step, which poses the question if Fe 'blocks' the available sites and may create more stable bonds. This effect, however, is less pronounced in Ni-PHI+Fe(II), where the final contents of Fe and Ni amount to 2.9 and 2.1 wt.%, respectively. Successive ion exchange, however, reduces the K content to ≈5.2 w.% in both materials, which is in accordance with the K content of Fe(II)-PHI-50 and Ni-PHI-50 (Figure 1).

To gain further insight into the PHI composition and uniformity on a microscopic scale, scanning electron microscopy (SEM) and transmission electron microscopy (TEM) with energy dispersive X-ray spectroscopy (EDX) were performed. For this purpose,

16146840, 0, Downloaded from https://advanced.onlinelibrary.wiley.com/doi/10.1002/aenm.202506308, Wiley Online Library on [05/02/2026]. See the Terms and Conditions (https://onlinelibrary.wiley.com/terms-and-conditions) on Wiley Online Library for rules of use; OA articles are governed by the applicable Creative Commons License

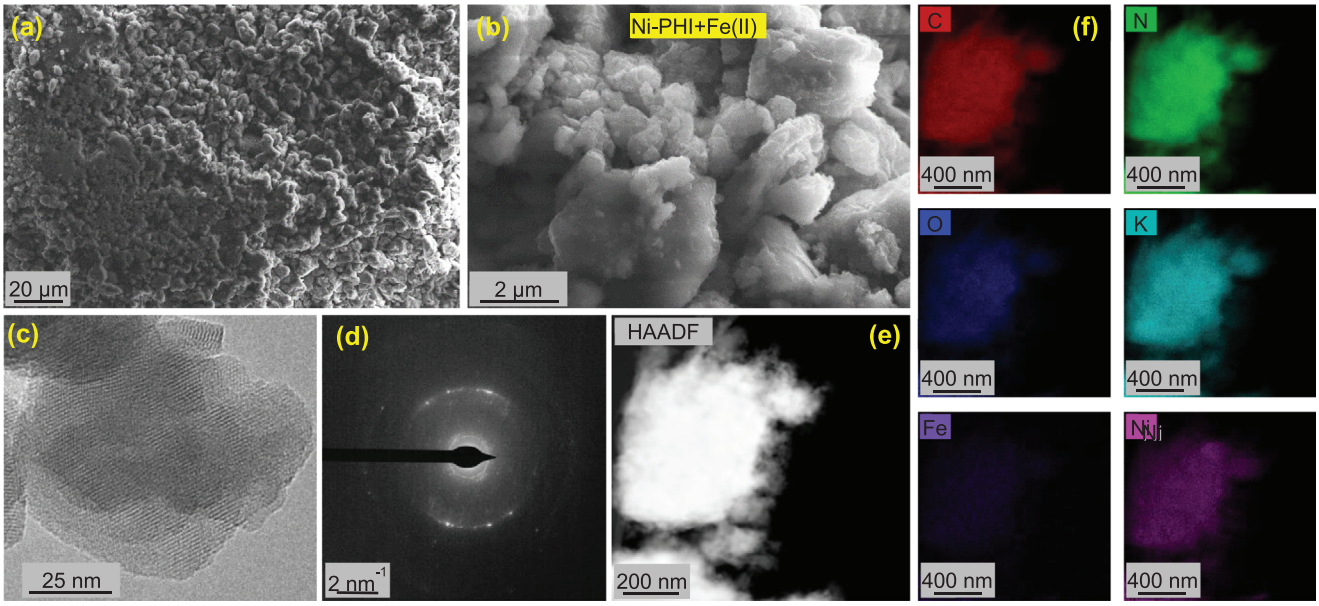

FIGURE 5 | (a-b) SEM micrographs of Ni-PHI+Fe(II). (c) HRTEM micrograph of Ni-PHI+Fe(II) with visible lattice fringes indicative of the layered PHI structure. (d) SAED pattern of Ni-PHI+Fe(II) shows strong spots at 1 and 3.4 nm^{-1}. (e) HAADF-TEM of Ni-PHI+Fe(II) combined with (f) STEM-EDX mapping of C, N, O, K, Fe and Ni indicating homogeneous distribution of the elements.

K-PHI, Fe(II)-PHI-10, Ni-PHI-10 (Figure S18) and Ni-PHI+Fe(II) (Figure 5) were investigated. The morphology of Ni-PHI+Fe(II) appears to be closely packed, with flakes of PHI having a low surface area (Figure 5a,b). SEM-EDX mapping of Ni-PHI+Fe(II) indicates that the elements are distributed homogenously within the material at the microscopic level (Figure S19).

In high-resolution TEM (HRTEM), lattice fringes are clearly visible, confirming the layered structure of PHIs (Figure 5c). In this context, however, it must be pointed out that M-PHIs are susceptible to electron beam damage, leading to rapid loss of crystallinity under irradiation (Figure S20). Regarding the parental K-PHI, C, N, O, and K are evenly distributed across the material as indicated by STEM-EDX mapping (Figure S18a). The obtained selected area electron diffraction (SAED) pattern shows that the crystallinity of the material is generally low (Figure S21). However, Ni-PHI+Fe(II) shows more pronounced diffraction, although deriving from K-PHI (Figure 5d). This observation, however, indicates the loss of crystallinity under the harsh conditions during TEM analysis, which results in sample degradation. Similar to the SEM-EDX mappings of Ni-PHI+Fe(II), the homogenous distribution of the elements can also be observed at a smaller scale via STEM-EDX analysis (Figure 5e,f). In Fe(II)-PHI-10, however, STEM-EDX mapping indicates the formation of Fe clusters (Figure S18), who show some correlation to the oxygen distribution. This could indicate the formation of Fe oxide or hydroxide within the PHI. Investigations of ORR and OER behavior of Fe_2O_3 do not indicate significant activity, which renders the contribution of this oxide species within Fe-PHIs unlikely (Figure S22).

This poses the question of which role the different Fe species take as electrocatalytic active species. Another explanation for the correlation of the Fe and O signal is the interaction of Fe with the structurally integrated water within the ionic channels. Regarding Ni(II)-PHI-10, aside from the aforementioned sharper diffraction patterns, nanostructures are observable in the HRTEM image, indicating the layered structure of the PHI network, which degrades rapidly under prolonged irradiation. Here, the distribution of C, N, O, as well as K and Ni, is homogeneous across the sample. For the mixed-metal Ni-PHI+Fe(II), the distribution of elements is homogeneous as well. Here, unlike in Fe(II)-PHI-10, no clustering of Fe is observable.

The ORR and OER activities were investigated by LSV measurements analogous to the single-TM PHIs (Figure 4, Figure S23). Regarding the ORR, no activity can be observed for all three mixed-metal PHIs, similar to the M-PHI-50 (Figure 4a). This suggests that the metal loading at the surface might be too high, and the ORR is kinetically hindered. For the OER, however, good activity can be observed for all three materials (Figure 4b). Here, Ni-PHI+Fe(II) is the superior candidate for the OER with an onset potential of 1.604 mV, surpassing the benchmark catalyst RuO_2 by ≈20 mV, as also indicated by Tafel slopes (Figure S24). As the performance even surpasses Ni-PHI-10, it can be hypothesized that the interaction of Ni and Fe results in higher catalytic performance.

2.5 | Application in a Zinc-Air Full Cell Battery Setup

After characterization of the M-PHI materials regarding their structural features as well as their performance for the electrocatalytic ORR and OER, the materials were employed in a ZAB full cell (Figure S25).

For this purpose, PHIs and conductive carbon black were drop-casted onto a gas diffusion layer (GDL) to a catalyst loading of 1 $mgcm^{-2}$ to fabricate the air cathode. As an electrolyte, an aqueous 6 M KOH + 0.25 M Zn^{2+} solution was used. Prior to

16146840, 0, Downloaded from https://advanced.onlinelibrary.wiley.com/doi/10.1002/aenm.202506308, Wiley Online Library on [05/02/2026]. See the Terms and Conditions (https://onlinelibrary.wiley.com/terms-and-conditions) on Wiley Online Library for rules of use; OA articles are governed by the applicable Creative Commons License

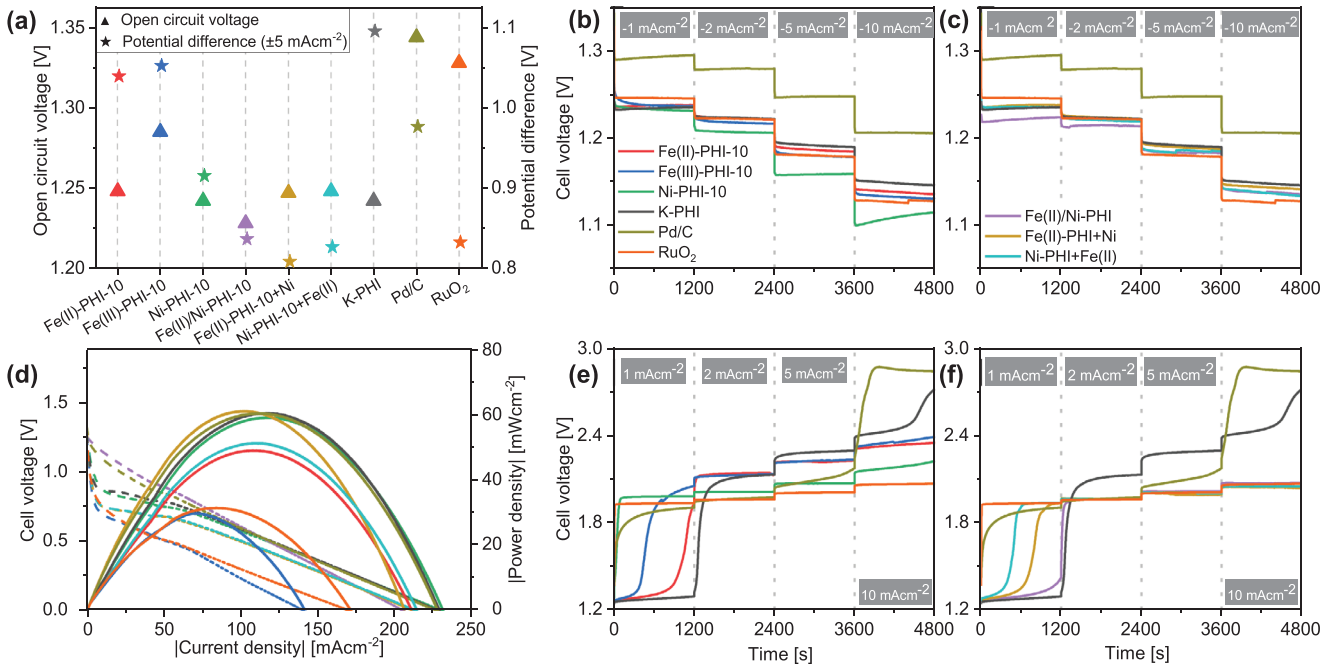

FIGURE 6 | (a) Open circuit voltages of the assembled cells prior to GCPL and potential differences of the OER and OER recorded half-way at ± 5 $mAcm^{-2}$. For discharge and charge curves, GCPL was performed at current densities of 1, 2, 5 and 10 $mAcm^{-2}$ for 20 min each. (b) Discharge curves of M-PHI-10, K-PHI, and the reference materials. (c) Discharge curves of mixed metal Fe(II)/Ni-PHIs, K-PHI, and the reference materials. (d) Voltage and power density plots. (e) Charge curves of M-PHI-10, K-PHI and the reference materials. (f) Charge curves of Fe(II)/Ni-PHIs, K-PHI, and the reference materials.

each test, the open circuit voltages (OCV) of the assembled batteries were measured. Here, the reference materials reach a cell voltage of ≈1.33 V vs. Zn/Zn^{2+}. The OCVs of the PHIs generally lie between 1.22–1.25 V, with Fe(III)-PHI-10 reaching 1.28 V, possibly due to the higher wettability of the electrode surface by interaction of Fe^{3+} with the electrolyte (Figure 6a). All OCVs are lower than the benchmark catalysts Pd/C and RuO_2, which could be related to the lower electric conductivity of the cathodes due to the semiconducting nature of PHI materials. Galvanostatic cycling with potential limitation (GCPL) was performed at current densities of ±1, 2, 5, and 10 $mAcm^{-2}$ to examine the discharge-charge behavior. The discharge curves indicate Pd/C as a high-performing catalyst for the discharge reaction as already indicated in the ORR performance in LSV measurements (Figure 6b). Generally, the discharge curves of the full cells containing different PHI materials at the cathode are comparable (Figure 6b,c). For all full cells, plateauing is achieved relatively fast. However, especially at higher current densities, differences due to the cathodes become more prominent. Ni-PHI-10 cathodes yield the lowest plateau voltages, comparable to the high overpotential observed in the ORR LSV curves. In opposite to this, the highest voltages are observed for K-PHI cathodes. However, since the onset potentials of the M-PHI-10 and K-PHI are comparable, as indicated by the LSV measurements, fluctuations within the measurements are possible, and the influence of metal within the PHI on the discharge performance is relatively low.

The discharge behavior of the tested cells is further characterized regarding their power density at increasing current densities (Figure 6d) [38, 42, 43]. The highest power densities are observed for Fe(II)-PHI+Ni, Ni-PHI-10, K-PHI, and Pd/C cathodes with ~60 $mWcm^{-2}$ at current densities of ~110 $mAcm^{-2}$. Full cell failure is observed for Ni-PHI-10, K-PHI, and Pd/C cathode at current densities of ≈230 $mAcm^{-2}$. Meanwhile, PHIs decorated with Fe^{2+}, more specifically using Fe(II)-PHI-10 and Ni-PHI+Fe(II) at the cathode side, yield full cells with lower maximum power and battery failure at ≈210 $mAcm^{-2}$. The lowest power density is observed for full cells containing Fe(III)-PHI-10, underlining the role of the metal's oxidation state for the ORR. Regarding the cell voltage over the course of the experiments, a significant drop in initial voltage can be observed at current densities of ≈5 $mAcm^{-2}$, where the diffusion of oxygen toward the GDL interface is not limited.

Regarding the charge curves of the full cells, more diverse results are observable. Here, the full cell using benchmark catalyst RuO_2 readily enters the plateau region at 1 $mAcm^{-2}$, while slower plateauing is notable for the use of PHI materials with the exception of Ni-PHI. Generally, higher charging voltages are observed for the cells with M-PHI-10 in reference to RuO_2 (Figure 6e,f). Charge voltages competing with the performance of RuO_2 are observable for the three mixed-metal PHIs. This emphasizes the potential of PHI materials as a noble-metal electrocatalyst alternative, as they exhibit promising ORR activity without optimization of the material yet. After charging at 1 mA cm^{-2}, plateauing occurs relatively fast. Since cells with the mixed-metal PHIs show lower charging voltages than Ni-PHI-10, a synergy between Fe- and Ni-sites might be possible; however, the origin of this synergy needs to be better understood in future studies. At low current densities of 1 mA cm^{-2}, especially cells with Fe-containing PHIs show the presence of slower electrochemical processes. It is speculated that this could originate from redox processes of $Fe^{2+/3+}$.

16146840, 0, Downloaded from https://advanced.onlinelibrary.wiley.com/doi/10.1002/aenm.202506308, Wiley Online Library on [05/02/2026]. See the Terms and Conditions (https://onlinelibrary.wiley.com/terms-and-conditions) on Wiley Online Library for rules of use; OA articles are governed by the applicable Creative Commons License

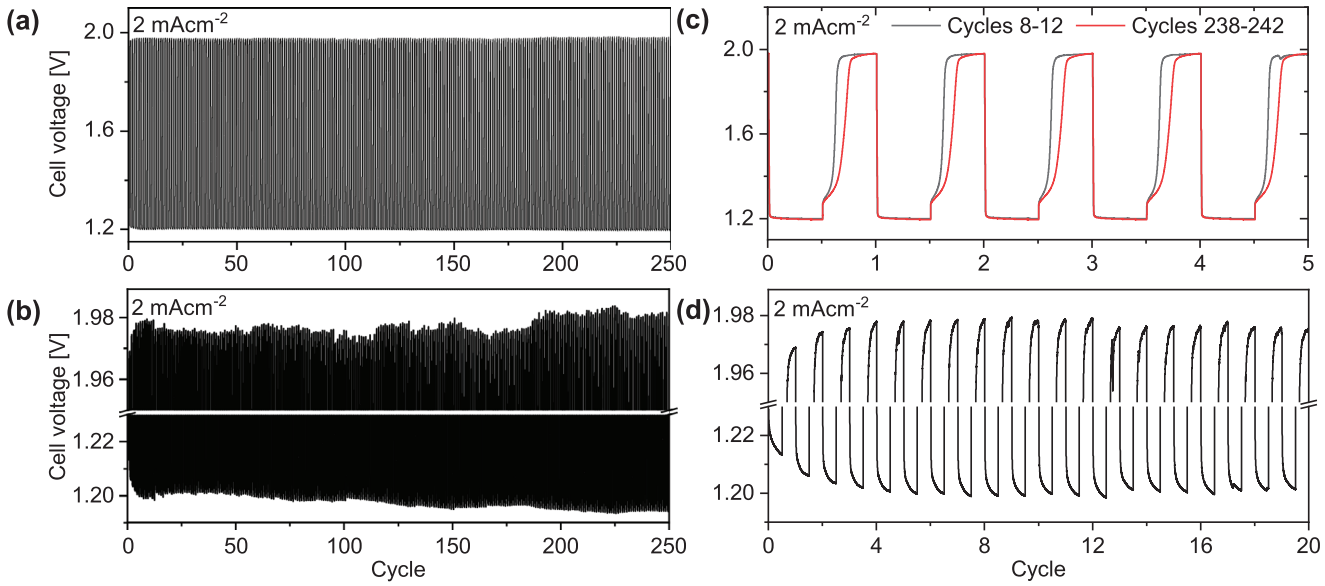

FIGURE 7 | Long-term galvanostatic cycling tests of Ni-PHI+Fe(II) performed in a ZAB setup at a current density of ±2 $mAcm^{-2}$ over 250 discharge-charge cycles. Each discharge-charge cycle was performed over 20 min. (a) GCPL curve of the experiment. (b) Close-up of the GCPL curve indicating the change of maximum charge and discharge potentials over time. (c) Cycles 8-12, and 238-242 superimposed. (d) Close-up view of the first 20 cycles.

To gain insight into the long-term stability of the best performing battery, the Ni-PHI+Fe(II) cell was subjected to a long-term discharge-charge cycling experiment (Figure 7). For the duration of the whole measurement, the discharge and charge potentials show minor fluctuations, yet no significant decrease of battery performance can be seen, which confirms the battery's stability (Figure 7a,b). By comparison of the discharge-charge cycles 8-12, and 238-242, it can be observed that plateauing occurs quickly during discharge, and the voltages remain the same (Figure 7c). During the charging process, however, the plateauing occurs more slowly toward the end of the experiments. This indicates that over time, the performance of the ZAB increases as the charging voltages decrease at the start of the charging process in later cycles. Initially, the discharge voltage lies at ≈1.21 V while the charge voltage lies at ≈1.97 V. Over the course of the first ten cycles, the discharge voltage decreases by ≈14 mV while the charge voltage increases by ≈8 mV (Figure 7d), indicating equilibration of the system.

3 | Summary and Outlook

The performance of transition metal functionalized poly(heptazine imides) (M-PHIs) for the electrocatalytic oxygen reduction reaction (ORR) and oxygen evolution reaction (OER) for application in a zinc-air battery (ZAB) setup was investigated in this study. The parental K-PHI was obtained by a facile two-step oven synthesis. Following aqueous ion exchange with Fe^{2+}, $Fe^{3+,}$ and Ni^{2+}, M-PHIs with low and high metal loading were obtained. Investigations by powder X-ray diffraction, inductively coupled plasma optical emission spectroscopy, and X-ray photoelectron spectroscopy reveal that the metal exchange mainly occurs at the PHI surface rather than the bulk material. Here, Fe-PHI (≈1 wt.% Fe) demonstrated good performance for the ORR while Ni-PHI (≈1 wt.%) excelled for the OER, competing with the noble metal catalyst RuO_2. Based on those results, mixed-transition-metal PHIs were synthesized by simultaneous ion exchange. In a ZAB setup, mixed-transition-metal PHIs exhibited promising bifunctional catalyst performance with a potential gap of ≈800 mV recorded at current densities of 5 $mAcm^{-2}$. Long-term cycling tests over 84 h and 250 discharge-charge cycles at 2 $mAcm^{-2}$ reveal excellent cycling stability, marking the presented materials as potential candidates for long-term applications.

Overall, this study presents M-PHI materials as scalable, low-cost electrocatalysts for sustainable energy storage systems. Future research could focus on optimizing the morphology of the materials in order to increase the relatively low-surface area and allow for better contact of active sites and electrolyte. In addition, due to their low conductivity, PHI/carbon hybrids offer the potential to combine the well-ordered structure of PHI with the electric conductivity of carbon, thus potentially increasing the overall electrocatalytic performance.

Acknowledgements

The authors acknowledge Stephanie Höppener and Ulrich S. Schubert for providing access to the scanning electron microscope. The SEM facilities of the Jena Center for Soft Matter (JCSM) were established with a grant from the DFG. The authors further thank the Carl-Zeiss-Stiftung for financial support for the project ReAlBatt (P2022-04-046) and the DFG for support within the project "FuncHeal" (FOR 5301). Robert Leiter and Simon Fleischmann acknowledge funding from the German Federal Ministry of Research, Technology, and Space (BMFTR) in the NanoMatFutur program (03XP0423) and basic funding from the Helmholtz Association. Sri Rezeki acknowledges the Center for Education Funding Services, Ministry of Education, Culture, Research, and Technology, Republic of Indonesia. Desirée Leistenschneider acknowledges fruitful discussions and scientific exchange with Prof. Martin Oschatz as well as access to his scientific infrastructure.

Open access funding enabled and organized by Projekt DEAL.

16146840, 0, Downloaded from https://advanced.onlinelibrary.wiley.com/doi/10.1002/aenm.202506308, Wiley Online Library on [05/02/2026]. See the Terms and Conditions (https://onlinelibrary.wiley.com/terms-and-conditions) on Wiley Online Library for rules of use; OA articles are governed by the applicable Creative Commons License

Conflicts of Interest

The authors declare no conflicts of interest.

Data Availability Statement

The data that support the findings of this study are openly available in Radar4Chem at https://doi.org/10.22000/230jp8d362w6w897, reference number [1].

References

1. S. Borsacchi and M. Peruzzini, "Electrochemistry: From Alessandro Volta's Genius to the Future," *Pure and Applied Chemistry* 95, no. 11 (2023): 1127, https://doi.org/10.1515/pac-2023-2010.

2. Y. Liu, X. Lu, F. Lai, et al., "Rechargeable Aqueous Zn-Based Energy Storage Devices," *Joule* 5 (2021): 2845–2903, https://doi.org/10.1016/j.joule.2021.10.011.

3. F. Wang, O. Borodin, T. Gao, et al., "Highly Reversible Zinc Metal Anode for Aqueous Batteries," *Nature Materials* 17, no. 6 (2018): 543–549, https://doi.org/10.1038/s41563-018-0063-z.

4. N. Shang, K. Wang, M. Wei, et al., "Challenges for Large Scale Applications of Rechargeable Zn–Air Batteries," *Journal of Materials Chemistry A* 10, no. 31 (2022): 16369–16389, https://doi.org/10.1039/D2TA04294K.

5. P. Pei, K. Wang, and Z. Ma, "Technologies for Extending Zinc–Air Battery's Cyclelife: A Review," *Applied Energy* 128 (2014): 315–324, https://doi.org/10.1016/j.apenergy.2014.04.095.

6. J. Goldstein, I. Brown, and B. Koretz, "New developments in the Electric Fuel Ltd. Zinc/AIR system," *Journal of Power Sources* 80, no. 1 (1999): 171–179, https://doi.org/10.1016/S0378-7753(98)00260-2.

7. A. R. Kottaichamy, J. Tzadikov, A. Pedersen, et al., "A Rechargeable Zn–Air Battery With High Energy Efficiency Enabled by a Hydrogen Peroxide Bifunctional Catalyst," *Advanced Energy Materials* 14, no. 47 (2024): 2403817, https://doi.org/10.1002/aenm.202403817.

8. B. Wu, H. Meng, D. M. Morales, et al., "Nitrogen-Rich Carbonaceous Materials for Advanced Oxygen Electrocatalysis: Synthesis, Characterization, and Activity of Nitrogen Sites," *Advanced Functional Materials* 32, no. 31 (2022): 2204137, https://doi.org/10.1002/adfm.202204137.

9. M. Lüsi, H. Erikson, A. Sarapuu, K. Tammeveski, J. Solla-Gullón, and J. M. Feliu, "Oxygen Reduction Reaction on Carbon-Supported Palladium Nanocubes in Alkaline Media," *Electrochemistry Communications* 64 (2016): 9.

10. L. Rostek, E. Pirard, and A. Loibl, "The Future Availability of Zinc: Potential Contributions From Recycling and Necessary Ones From Mining," *Resour Conserv Recycl Adv* 19 (2023): 200166.

11. D. Böhm, M. Beetz, C. Gebauer, et al., "Highly Conductive Titania Supported Iridium Oxide Nanoparticles With Low Overall Iridium Density as OER Catalyst for Large-Scale PEM Electrolysis," *Appl Mater Today* 24 (2021): 101134.

12. N. R. Sahraie, U. I. Kramm, J. Steinberg, et al., "Quantifying the Density and Utilization of Active Sites in Non-Precious Metal Oxygen Electroreduction Catalysts," *Nature Communications* 6, no. 1 (2015): 8618, https://doi.org/10.1038/ncomms9618.

13. D. Aasen, M. P. Clark, and D. G. Ivey, "Investigation of Transition Metal-Based (Mn, Co, Ni, Fe) Trimetallic Oxide Nanoparticles on N-doped Carbon Nanotubes as Bifunctional Catalysts for Zn-Air Batteries," *Journal of The Electrochemical Society* 167, no. 4 (2020): 040503, https://doi.org/10.1149/1945-7111/ab7094.

14. M. Ye, S. Li, X. Zhao, et al., "Cobalt-Exchanged Poly(Heptazine Imides) as Transition Metal–N x Electrocatalysts for the Oxygen Evolution Reaction," *Advanced Materials* 32, no. 9 (2020): 1903942, https://doi.org/10.1002/adma.201903942.

15. J. Liebig, "Über Einige Stickstoff-Verbindungen," *Ann Pharm* 10 (1834): 1–47.

16. C. M. Pelicano and M. Antonietti, "Metal Poly(Heptazine Imides) as Multifunctional Photocatalysts for Solar Fuel Production," *Angewandte Chemie International Edition* 63, no. 24 (2024): 202406290, https://doi.org/10.1002/anie.202406290.

17. A. Savateev, S. Pronkin, M. G. Willinger, M. Antonietti, and D. Dontsova, "Toward Organic Zeolites and Inclusion Catalysts: Heptazine Imide Salts Can Exchange Metal Cations in the Solid State," *Chemistry—An Asian Journal* 12, no. 13 (2017): 1517–1522, https://doi.org/10.1002/asia.201700209.

18. V. W. Lau and B. V. Lotsch, "A Tour-Guide Through Carbon Nitride-Land: Structure- and Dimensionality-Dependent Properties for Photo(Electro)Chemical Energy Conversion and Storage," *Advanced Energy Materials* 12, no. 4 (2022): 2101078, https://doi.org/10.1002/aenm.202101078.

19. W. Wang, Z. Shu, Z. Liao, et al., "Sustainable One-Step Synthesis of Nanostructured Potassium Poly(Heptazine Imide) for Highly Boosted Photocatalytic Hydrogen Evolution," *Chemical Engineering Journal* 424 (2021): 130332, https://doi.org/10.1016/j.cej.2021.130332.

20. W. Wang, X. Fan, Z. Shu, J. Zhou, and D. Meng, "Sustainable and Mild Exfoliation of Bulk Crystalline Carbon Nitride Into Ultrathin Nanosheets Via Ion-Exchange in Pure-Water," *Carbon* 205 (2023): 76–85, https://doi.org/10.1016/j.carbon.2023.01.002.

21. V. W. Lau, I. Moudrakovski, T. Botari, et al., "Rational Design of Carbon Nitride Photocatalysts by Identification of Cyanamide Defects as Catalytically Relevant Sites," *Nature Communications* 7, no. 1 (2016): 12165, https://doi.org/10.1038/ncomms12165.

22. J. Kröger, A. Jiménez-Solano, G. Savasci, et al., "Interfacial Engineering for Improved Photocatalysis in a Charge Storing 2D Carbon Nitride: Melamine Functionalized Poly(Heptazine Imide)," *Advanced Energy Materials* 11, no. 6 (2021): 2003016.

23. H. Schlomberg, J. Kröger, G. Savasci, et al., "Structural Insights Into Poly(Heptazine Imides): A Light-Storing Carbon Nitride Material for Dark Photocatalysis," *Chemistry of Materials* 31, no. 18 (2019): 7478–7486, https://doi.org/10.1021/acs.chemmater.9b02199.

24. G. Seo, Y. Saito, M. Nakamichi, K. Nakano, K. Tajima, and K. Kanai, "Mechanism of Charge Accumulation of Poly(Heptazine Imide) Gel," *Scientific Reports* 11, no. 1 (2021): 17833, https://doi.org/10.1038/s41598-021-97025-9.

25. X.-W. Guo, S.-M. Chen, H.-J. Wang, et al., "Single-Atom Molybdenum Immobilized on Photoactive Carbon Nitride as Efficient Photocatalysts for Ambient Nitrogen Fixation in Pure Water," *Journal of Materials Chemistry A* 7, no. 34 (2019): 19831–19837, https://doi.org/10.1039/C9TA06653E.

26. Q. Zhao, Q. Cai, Y. Li, et al., "Single-Atom Mo Anchored on a Poly(Heptazine Imide) Nanosheet as a Novel Electrocatalyst Showing Excellent Behavior Toward Nitrogen Reduction Reaction," *The Journal of Physical Chemistry C* 126, no. 18 (2022): 7859–7869, https://doi.org/10.1021/acs.jpcc.2c00312.

27. G. F. S. R. Rocha, M. A. R. Da Silva, A. Rogolino, et al., "Carbon Nitride Based Materials: More Than just a Support for Single-Atom Catalysis," *Chemical Society Reviews* 52, no. 15 (2023): 4878–4932, https://doi.org/10.1039/D2CS00806H.

28. M. A. R. Da Silva, I. F. Silva, Q. Xue, et al., "Sustainable Oxidation Catalysis Supported By Light: Fe-poly(Heptazine Imide) as a Heterogeneous Single-Atom Photocatalyst," *Applied Catalysis B: Environment and Energy* 304 (2022): 120965.

29. L. Xing, Q. Yang, C. Zhu, et al., "Poly(Heptazine Imide) Ligand Exchange Enables Remarkable Low Catalyst Loadings in Heterogeneous Metallaphotocatalysis," *Nature Communications* 14, no. 1 (2023): 1501, https://doi.org/10.1038/s41467-023-37113-8.

30. C. M. Pelicano, J. Li, M. Cabrero-Antonino, et al., "Rational Design of a Carbon/Potassium Poly(Heptazine Imide) Heterojunction for Enhanced

16146840, 0, Downloaded from https://advanced.onlinelibrary.wiley.com/doi/10.1002/aenm.202506308, Wiley Online Library on [05/02/2026]. See the Terms and Conditions (https://onlinelibrary.wiley.com/terms-and-conditions) on Wiley Online Library for rules of use; OA articles are governed by the applicable Creative Commons License

Photocatalytic H 2 and H 2 O 2 Evolution," *Journal of Materials Chemistry A* 12, no. 1 (2024): 475–482, https://doi.org/10.1039/D3TA05701A.

31. A. Rogolino, I. F. Silva, N. V. Tarakina, et al., "Modified Poly(Heptazine Imides): Minimizing H 2 O 2 Decomposition to Maximize Oxygen Reduction," *ACS Applied Materials & Interfaces* 14, no. 44 (2022): 49820–49829, https://doi.org/10.1021/acsami.2c14872.

32. A. Sivo, V. Ruta, V. Granata, O. Savateev, M. A. Bajada, and G. Vilé, "Nanostructured Carbon Nitride for Continuous-Flow Trifluoromethylation of (Hetero)Arenes," *ACS Sustainable Chemistry & Engineering* 11, no. 13 (2023): 5284–5292, https://doi.org/10.1021/acssuschemeng.3c00176.

33. M. A. R. Da Silva, N. V. Tarakina, J. B. G. Filho, et al., "Single-Atoms on Crystalline Carbon Nitrides for Selective C—H Photooxidation: A Bridge to Achieve Homogeneous Pathways in Heterogeneous Materials," *Advanced Materials* 35, no. 52 (2023): 2304152, https://doi.org/10.1002/adma.202304152.

34. Y. Markushyna, C. M. Schüßlbauer, T. Ullrich, D. M. Guldi, M. Antonietti, and A. Savateev, "Chromoselective Synthesis of Sulfonyl Chlorides and Sulfonamides With Potassium poly(Heptazine Imide) Photocatalyst," *Angewandte Chemie International Edition* 60, no. 37 (2021): 20543–20550, https://doi.org/10.1002/anie.202106183.

35. B. Chen, W. Lu, P. Xu, and K. Yao, "Potassium Poly(heptazine imide) Coupled With Ti 3 C 2 MXene-Derived TiO 2 as a Composite Photocatalyst for Efficient Pollutant Degradation," *ACS Omega* 8, no. 12 (2023): 11397–11405, https://doi.org/10.1021/acsomega.3c00150.

36. B. V. Lotsch, M. Döblinger, J. Sehnert, et al., "Unmasking Melon by a Complementary Approach Employing Electron Diffraction, Solid-State NMR Spectroscopy, and Theoretical Calculations—Structural Characterization of a Carbon Nitride Polymer," *Chemistry—A European Journal* 13, no. 17 (2007): 4969–4980, https://doi.org/10.1002/chem.200601759.

37. T. L. Barr and S. Seal, "Nature of the Use of Adventitious Carbon as a Binding Energy Standard," *Journal of Vacuum Science & Technology A: Vacuum, Surfaces, and Films* 13, no. 3 (1995): 1239–1246, https://doi.org/10.1116/1.579868.

38. Z. Abedi, D. Leistenschneider, W. Chen, and D. G. Ivey, "Spinel-Type Mn–Co Oxide Coated Carbon Fibers as Efficient Bifunctional Electrocatalysts for Zinc–Air Batteries," *Batteries Supercaps* 5, no. 2 (2022): 202100339.

39. I. F. Teixeira, E. C. M. Barbosa, S. C. E. Tsang, and P. H. C. Camargo, "Carbon Nitrides and Metal Nanoparticles: From Controlled Synthesis to Design Principles for Improved Photocatalysis," *Chemical Society Reviews* 47, no. 20 (2018): 7783–7817, https://doi.org/10.1039/C8CS00479J.

40. M. Mazzucato and C. Durante, "Toward More Practical Site Density Determination in Fe-N-C Catalysts for Oxygen Reduction Reaction: NO-Stripping at Gas Diffusion Electrode Setup," *Electrochimica Acta* 507 (2024): 145194, https://doi.org/10.1016/j.electacta.2024.145194.

41. J. Barrio, A. Pedersen, S. C. Sarma, et al., "FeNC Oxygen Reduction Electrocatalyst With High Utilization Penta-Coordinated Sites," *Advanced Materials* 35, no. 14 (2023): 2211022, https://doi.org/10.1002/adma.202211022.

42. Z. Abedi, J. Cui, W. Chen, and D. G. Ivey, "Zinc–Air Batteries With an Efficient and Stable $MnCo_2O_4$/Carbon Fiber Bifunctional Electrocatalyst and a Poly(acrylic Acid)-Based Gel Electrolyte," *ACS Applied Energy Materials* 5, no. 11 (2022): 14164–14174, https://doi.org/10.1021/acsaem.2c02699.

43. Z. Qiu, X. Guo, S. Cao, et al., "High-Entropy Ag–Ru-Based Electrocatalysts With Dual-Active-Center for Highly Stable Ultra-Low-Temperature Zinc-Air Batteries," *Angewandte Chemie International Edition* 64, no. 3 (2025): 202415216, https://doi.org/10.1002/anie.202415216.

Supporting Information

Additional supporting information can be found online in the Supporting Information section.

Supporting File: aenm70627-sup-0001-SuppMat.pdf.

16146840, 0, Downloaded from https://advanced.onlinelibrary.wiley.com/doi/10.1002/aenm.202506308, Wiley Online Library on [05/02/2026]. See the Terms and Conditions (https://onlinelibrary.wiley.com/terms-and-conditions) on Wiley Online Library for rules of use; OA articles are governed by the applicable Creative Commons License